Technical validation studies of a dual-wavelength LED-based photoacoustic and ultrasound imaging system

James Joseph[1,2,5], Mithun Kuniyil Ajith Singh[3], Naoto Sato[4] and Sarah E. Bohndiek[1,2]

[1] Department of Physics, University of Cambridge, JJ Thomson Avenue, Cambridge, CB3 0HE, U.K.

[2] Cancer Research UK Cambridge Institute, University of Cambridge, Robinson Way, Cambridge, CB2 0RE, U.K.

[3] Research and Business Development Division, CYBERDYNE INC, Rotterdam, 3013 AK, The Netherlands

[4] Research and Development Division, CYBERDYNE INC, Tsukuba, 305-0818, Japan

[5] Now at School of Science and Engineering, Fulton Building, University of Dundee, DD1 4HN, U.K.

Corresponding Author: Sarah E Bohndiek (seb53@cam.ac.uk)

Keywords: photoacoustics; light emitting diodes; phantoms.

Abstract

Recent advances in high power, pulsed, light emitting diodes (LEDs) have shown potential as fast, robust and relatively inexpensive excitation sources for photoacoustic imaging (PAI), yet systematic characterization of performance for biomedical imaging is still lacking. We report here technical and biological validation studies of a commercial dual-wavelength LED-based PAI and ultrasound system. Phantoms and small animals were used to assess temporal precision. In phantom studies, we found high temporal stability of the LED-based PAI system, with no significant drift in performance observed during 6 hours of operation or over 30 days of repeated measurements. *In vivo* dual-wavelength imaging was able to map the dynamics of changes in blood oxygenation during oxygen-enhanced imaging and reveal the kinetics of indocyanine green contrast agent inflow after intravenous administration (T_{max}~6min). Taken together, these studies indicate that LED-based excitation could be promising for future application in functional and molecular PAI.

Introduction

Photoacoustic imaging (PAI) is an exciting new modality for molecular imaging, which refers to the visualization, characterization and measurement of biological processes at the molecular and cellular levels in living subjects [1]. PAI reveals optical contrast at high spatio-temporal resolution by acoustically detecting optical absorption through the photoacoustic effect [2-4] . The unique capability of PAI to combine rich optical contrast with high ultrasonic spatial resolution in a single modality has proven advantageous for molecular imaging and led to wide adoption in studies ranging from fundamental biological sciences to clinical translational applications [5-8]. By performing PAI at multiple wavelengths, it is possible to resolve the selective light absorption of endogenous molecular imaging chromophores, such as hemoglobin, lipids and melanin, from those administered as exogenous contrast agents for both functional and molecular imaging [9]. Inspired by progress in other fields, recent studies in PAI have demonstrated clear capability for functional imaging, using oxygen-enhanced and dynamic-contrast-enhanced approaches in particular [10-12], as well as for targeted molecular imaging, exploiting state-of-the-art nanostructures and encapsulation designs [13-15].

One challenge that remains for widespread uptake of PAI is the reliance on relatively slow, fragile and expensive nanosecond pulsed lasers as excitation sources. While lasers can provide high pulse excitation power along with tunable output wavelengths, they typically result in bulky systems that require regular maintenance and their biomedical application requires compliance with laser safety standards for both the subject under study and also for the environment in which the study is undertaken. Furthermore, some contrasts agents including plasmonic nanoparticles are observed to be less stable when used in laser-based PAI systems [16, 17]. Advances in solid-state device technology have resulted in the development of several solutions for relatively fast, robust and low-cost excitation sources for PAI, such as pulsed laser diodes (PLDs) and high-power light emitting diodes (LEDs) [18]. In particular, commercial LED-based PAI devices have proven attractive for a range of

in vivo molecular imaging applications, from stem cell imaging to evaluation of arthritis, and interventional procedures [18-27]. Such early promise suggests LED-based PAI has the potential to be adopted as a preclinical and clinical imaging tool, yet systems need to undergo a thorough technical and biological validation prior to being used for longitudinal studies in the biomedical setting [28]. Prior work has focused on evaluating the LED beam profile, available resolution and penetration depth for imaging, as well as contrast agent sensitivity but as yet, temporal precision for performing functional and molecular imaging has not been evaluated.

Here, we report technical and biological validation studies of a dual-wavelength LED-based PAI and ultrasound imaging system that has the potential to perform real-time *in vivo* imaging. Our studies aimed to evaluate the temporal precision of the system for application to dynamic and longitudinal *in vivo* imaging. Evaluation of precision was performed in phantoms and *in vivo*. Measurements were made in tissue-mimicking phantoms to independently assess the impact of system variables on precision, including sample positioning and frame averaging. Temporal variation was assessed by repeated measurements over minutes, hours and days in the phantoms. *In vivo* studies were then made using small animals for biological validation of the system using both oxygen-enhanced and dynamic contrast-enhanced imaging.

Materials and Methods

LED-based photoacoustic imaging

A commercial LED-based photoacoustic (PA) and ultrasound (US) imaging system (Acoustic X, CYBERDYNE INC., Japan) was used in this study. The system performs interleaved PA and US (planewave or line-by-line scan) measurements at video rate using LED arrays as the excitation sources for PAI. In this work, we used a combinational two-wavelength LED array operating at 750 and 850 nm. Each LED array consists of 120 elements, in which first and third rows are embedded with 850 nm LED elements (36 elements in a row) and second and fourth rows with 750 nm elements (24 elements per row). Energy per pulse is 50 μJ, and 100 μJ for 750 nm and 850 nm respectively and the LEDs were driven at their maximum pulse repetition rate (PRR) of 4 KHz [22, 29]. A pair of LED arrays were fixed on both sides of a linear array US probe [22], which covers the whole aperture of the linear array US probe (38.4 mm) and provides an illumination area of 50 mm × 7mm onto the sample surface. The illumination pulse duration (full width at half maximum) of LED light is tunable and can be varied from 30 – 100 ns; 70 ns was used in this study.

Ultrasound detection and processing

US detection was performed with a linear-array PZT-based probe composed of 128 elements, each with a transverse aperture of 5 mm and a pitch of 0.315 mm. The array has a central frequency of 7 MHz and a measured −6 dB bandwidth of 80%. The array incorporates an acoustic lens to focus the US in the elevational plane at about 20 mm. For LED-based PAI, raw radiofrequency (RF) data from all US elements are acquired at sampling rates of 40 MHz and 20 MHz respectively for US and PA imaging and transferred to the computer graphical processing unit board using USB 3.0 interface. Acquired data (US and PA) are reconstructed using a system integrated Fourier-domain based reconstruction algorithm [30] for real-time display. The high pulse repetition rate (4 KHz) of the LED

excitation sources affords the ability to perform averaging to enhance the signal to noise ratio (SNR) while maintaining real-time frame rates. When frame averaging of 128 frames is performed, the display frame rate is 30Hz; this reduces to 1.5Hz when 2560 photoacoustic frames are averaged. The frame rate was controlled in real-time based on the SNR obtained during experiments, except in experiments where the SNR was the variable under test. After each measurement, raw RF data (PA and US) were saved for further offline processing.

Gantry for evaluating precision of LED-based photoacoustic imaging

To perform precision evaluations in phantoms and *in vivo*, a gantry was designed to mount the handheld ultrasound probe with LED arrays, minimizing the influence of the human operator on the studies (Fig. 1A, B). The gantry was composed of a motorized laboratory jack for z positioning (MLJ150/M, Thorlabs) and two translation stages for x,y positioning (OSMS20-8, Sigmakoki, Corp). The probe was mounted within a custom holder and attached to the manual (x,y,z) positioning stages. A custom acrylic water bath was mounted onto the same breadboard (MB3045/M, Thorlabs, Inc.) containing an aluminum phantom holder for phantom imaging; a second custom water bath (fabricated using acrylic side walls and polyethylene membrane base) and temperature-maintained animal bed with infrared heat pad were used for *in vivo* imaging (Fig. 1C, D). Once mounted in either setup, the probe could be raised and lowered onto the imaged samples using the motorized laboratory jack.

Precision evaluation in phantoms

Polyvinyl chloride plastisol (PVCP) phantom bulk material was used to fabricate a stable phantom used for precision evaluation. The mechanical, optical and ultrasound properties of PVCP have been reported previously [31-33]. Briefly, the phantom base material was composed of commercial polyvinyl chloride plastisol (PVCP; M-F Manufacturing Co, USA) with black plastic color (BPC; M-F Manufacturing Co, USA) to provide an absorption coefficient μ_a of 0.05cm^{-1} and titanium oxide (TiO_2) powder (232033; Sigma-Aldrich, UK) to give a reduced scattering coefficient μ'_s of 5 cm^{-1} based on our prior

work [31]. The base material mixture was heated under vacuum until the phase transition was complete and poured into a custom phantom mold in which cylindrical holes of 3 mm diameter were formed at ~1.2 cm below the phantom surface. These cylindrical holes were used to place sealed thin-walled plastic straws containing solutions of the light absorbing dye nigrosin (198285; Merck, UK) at 0.5 $mgmL^{-1}$ to form the target inclusions for precision evaluation or the fluorescent dye indocyanine green (ICG, I2633; Sigma-Aldrich, UK) at a range of concentrations to test sensitivity prior to *in vivo* imaging.

The phantom mold was mounted into the phantom holder, which ensured repeated positioning, and placed into the custom water bath at room temperature. Phantoms were allowed to attain temperature equilibrium with the water bath before any imaging was performed. Following temperature equilibration of the phantom, images were acquired from the target inclusions at 750 nm and 850 nm. The stability of the system was assessed over 180 minutes and the repeatability in longitudinal studies was measured over the course of 6 hours, 1 day and 1 month. The impact of averaging on signal to noise ratio (SNR) and signal to background ratio (SBR) was also assessed using the same phantom.

Precision evaluation in vivo

Procedures in small animals were carried out in accordance with project (70-8214) and personal licenses (IFBB827BC) issued under the United Kingdom Animals (Scientific Procedures) Act, 1986. The procedures were reviewed by the Animal Welfare and Ethical Review Board at the CRUK Cambridge Institute under compliance form number CFSB1232V2. Healthy female BALB/c nude mice aged between 8 and 12 weeks were housed in techniplast green line IVC cages with APB6 bedding on 12 hours on/off light/dark cycle (7am to 7pm).

For imaging in living subjects, evaluation of precision was made separately across oxygen enhanced and dynamic contrast enhanced parameters, according to the following standard operating procedure. Briefly, mice were anaesthetized using <2.5% isoflurane in 100% oxygen and placed on a heat pad. Administration of contrast agents was carried out

using a catheter (home-made with 30G needle) placed into the tail vein and fixed in place using tissue glue (TS1050071F; TissueSeal). The respiratory rate of the animals was maintained within range 70–80 b.p.m. by modulating the isoflurane concentration (1.5-2.5% isoflurane concentration) as required during the entire scan. Mice were placed supine over a far infrared heating pad (Kent Scientific Corp, USA). The far infrared heating pad ensured efficient and safe warming of the animal throughout the entire imaging procedure.

The LED-based PA/US probe was placed inside a custom water bath made with a layer of flexible polyethylene membrane forming the base of the imaging chamber. A thin layer of clear ultrasound gel (Aquasonics, Parker Laboratories Inc, USA) was applied over the skin of the mouse to provide acoustic coupling between the animal body and the polyethylene membrane of the imaging chamber. Imaging was performed in a single slice centered on the liver. Oxygen enhanced PA studies were performed at 750nm and 850nm excitation (0.75 frames per second, 5320 frame averages) with breathing gas modulated between medical air (21% oxygen) and pure oxygen (100% oxygen) using separate flow meters. The combination LED array (750 nm and 850 nm) allows wavelength switching at a repetition rate of 4 KHz, so frame averaging could be performed to improve the SNR without compromising the image frame rate. Animals (n=2) were subjected to 3 modulation cycles (medical air to pure oxygen) of breathing air. One week later, dynamic contrast-enhanced studies were performed in the same animals. ICG was chosen for these studies as it is an FDA approved and water-soluble dye that has been widely used for a variety of clinical endpoints, such as hepatic function [34] and is commonly used in PAI studies. Mice were initially allowed to stabilize their physiology for 10 minutes. After 30 seconds of continuous imaging at 750nm excitation (0.75 frames per second, 5320 times averaging) to establish the baseline PA signal, ICG (48 nmol, selected based on prior studies linking *in vitro* and *in vivo* detectability [28, 35]) was administered intravenously through the tail vein catheter. PAI image acquisition at 750nm excitation was continued for a further 15 minutes to extract the dynamics and signal enhancement curve.

Image and statistical analysis

Images were reconstructed offline as mentioned above using a previously reported Fourier-domain reconstruction algorithm [30] and analyzed in MATLAB 2017b (Mathworks) using custom software and the envelope of images (PA and US) were plotted in linear amplitude scale. Image reconstruction assumed a constant speed of sound in the medium, being 1450 ms^{-1} for phantom studies (based on the sound speed in PVCP) and 1540 ms^{-1} for animal experiments (based on the soft tissue average). The use of a single sound speed may impact the depth of reconstructed features in the case of inhomogeneous speed of sound inside the test object. Pixel size in the axial and lateral directions of both PA and US images were 40 μm and 315 μm respectively. Images were normalized by the pulse energy. Regions of interest (ROI) were drawn manually around the targets of interest and mean pixel intensity (MPI) values were extracted from the ROIs. For phantom studies, images obtained at 750 nm and 850 nm excitation wavelengths were used with the position and size of signal and background ROIs set identically across all data sets. SNR was calculated as the ratio of the mean of the signal ROI to the standard deviation of the background ROI. Signal-to-background ratio (SBR) was calculated as the ratio of the mean of the signal ROI to the mean of the background ROI.

For small animal imaging studies, ROIs were drawn around the liver region of each mouse. Dual wavelength (750nm and 850nm) images were used to infer the relative oxygenation of the hemoglobin in the tissue during the OE experiment. PA-based oximetry relies on the spectroscopic differences between oxyhemoglobin (HbO_2) and deoxyhemoglobin (Hb). Since HbO_2 and Hb are the dominant absorbing compounds in a nude mouse in the spectral region under study, the PA measurements of the animal at 850 nm and 750 nm respectively were considered sufficient to evaluate relative oxygenation without compensating for the local fluence [36]. Since PAI is not able to measure absolute SO_2 without an accurate knowledge of local optical energy distribution, the SO_2 metric used in this study is only relative and we denote this as SO_2^{PAI}; the average SO_2^{PAI} for medical air and oxygen breathing periods are denoted as SO_2^{PAI} (Air) and SO_2^{PAI} (Oxygen) respectively.

SO_2^{PAI} values for each pixel were calculated by taking the ratio of the 850 nm image to the sum of that from 750 nm and 850nm. For the dynamic contrast enhanced experiment, the 750 nm images were analyzed and the extracted metrics included: time to half maximum ($T_{1/2}$), which gives the time taken for the signal to rise from baseline to 50% of maximum intensity; and time to maximum (T_{max}), the time taken for the signal to rise from baseline to the maximum intensity.

Coefficients of variation (COV) were calculated from the raw MPI values extracted from the ROIs as the ratio of the standard deviation to the mean and expressed as a percentage. Uncertainty on mean values is represented by the standard error unless otherwise stated. Statistical analysis was performed in Origin (OriginLab Corp.). Linear regression analysis was performed in Origin and P-value < 0.05 was considered as statistically significant.

Results

Longitudinal imaging in a stable phantom showed high precision of the LED-based PAI system.

We first evaluated the longitudinal imaging performance of the system in phantoms (Fig. 2A) over 180 minutes (without replacement), 6 hours (with and without replacement) and 30 days (with replacement) using the 750/850 nm combinational LED array. The temporal stability of the LED-based photoacoustic imaging system for over 180 minutes in phantoms was found to be excellent: the slopes of the linear fits to the data acquired over 180 minutes were not statistically different from zero, indicating negligible system drift (Fig. 2B). Further, the extended study over 30 days resulted in coefficients of variation (COVs) of only 7.0% and 5.8% respectively for 750nm and 850nm excitation wavelengths (Fig 2C) with no significant system drift. Within the 6 hour study, we examined the influence of sample replacement on the data, by removing and replacing the phantom in one study (Fig. 2D), and leaving it within the imaging system in a second (Fig. 2E). The COVs over 6 hours at 750nm and 850nm were found to be 1.9% and 1.2% respectively with replacement and 1.5% and 1.2% respectively without replacement. No significant system drift was observed in the mean pixel intensity extracted from the signal ROI during the course of 6 hours.

Enhancement of image quality is observed through averaging LED pulses while maintaining real-time imaging.

We then confirmed the impact of frame averaging on the measured image signal-to-noise ratio (SNR) and signal-to-background ratio (SBR) using the same phantom. As expected, frame averaging results in an increase of image SNR and SBR at both 750 nm (Fig. 3A, B) and 850 nm (Fig. 3C, D). We noted a slight dip in performance for the 850 nm LED at around 25,000 averages, which may be due to an unanticipated source for experimental error in our data given that the error bars are contained within the symbols for this plot. In both cases, a threshold above which further averaging did not substantially

improve performance was reached: for 750nm this occurred at 20,000 averages whereas for 850 nm this was already the case at 10,000 averages. At this level of averaging (i.e. maximal SNR and SBR) the frame rate would be 0.1 and 0.2 Hz respectively at 750 nm and 850 nm, yet operation could be maintained at 0.75 Hz with 5320 frame averaging, which still represents an increase of 35-fold in SNR, 16-fold in SBR and 280-fold in SNR, 265-fold in SBR compared to no averaging at 750 nm and 850 nm respectively.

The LED-based system can perform oxygen enhanced PAI.

Following our phantom studies, we commenced studies to test temporal precision of the readout provided by LED-based PAI in oxygen enhanced hemoglobin imaging. We selected 2660 averages for imaging at 0.75 Hz at both wavelengths based on our phantom experiments, which was reasonable based on the anticipated kinetics of the data we would be recording. Dynamic data was recorded while the mice breathed either medical air (Movie 1) or 100% oxygen (Movie 2). By extracting the data available from dual wavelength imaging (Hb at 750nm and HbO_2 at 850nm), SO_2^{PAI} was estimated across multiple breathing cycles exploiting the high temporal resolution of the system. The results allowed us to evaluate the precision with which LED-based PAI could extract changes in oxygen saturation in the liver. SO_2^{PAI} maps of the liver showed clear variations in SO_2^{PAI} levels during oxygen enhancement, while the mouse was breathing either medical air or pure oxygen (Fig. 4A). The dynamics of SO_2^{PAI} over time under multiple breathing cycles (Fig. 4B) were then extracted for all mice (Table 1). These dynamic studies yielded COV values of 2.9% for SO_2^{PAI} (Air) and 3.5% for SO_2^{PAI} (Oxygen) within same mouse and 7.6% for SO_2^{PAI} (Air) and 10% for SO_2^{PAI} (Oxygen) across replicates (n=2). The consistency of the change in blood oxygenation levels (ΔSO_2) under different breathing cycles indicates that, as with other PAI studies [10, 29], a high precision is available for the system in measuring changes in blood oxygenation (within one mouse) and with studies across multiple mice, indicates the inherent biological variation between living subjects.

Dynamic contrast enhanced imaging detects uptake of indocyanine green in the liver.

Finally, we performed *in vivo* LED-based PAI in the liver region after administration of indocyanine green, to assess the ability of the system to monitor the uptake of exogenous contrast agents. We first placed solutions of ICG into the stable phantom and determined the limit of detection for ICG to be 5μM at 1 cm depth in the phantom. We then acquired *in vivo* PA signals at 750 nm excitation wavelength, which clearly showed an increase in the PA signal within the liver from the baseline (Fig. 5A) over time following administration of ICG (Fig. 5B). The signal enhancement curves (Fig. 5B) gave $T_{1/2}$ and T_{max} values of ~2.2 minutes and ~5 minutes respectively, showing the dynamic mapping of the changes in the uptake of indocyanine green and in a close agreement with a previously reported study that used a laser-based PAI system [35].

Discussion

PAI is a rapidly evolving hybrid optical imaging modality that offers high spatio-temporal resolution and deep tissue imaging capabilities with optical contrast. The combined functional and molecular imaging capability of PAI makes it a promising imaging technology for biomedical applications, however, the reliance on bulky, expensive and fragile pulsed lasers, with their associated safety requirements, has led to a demand for more portable and inexpensive LED-based systems. The aim of this work was to evaluate the suitability of an LED-based PAI system for molecular imaging in small animals by assessing the temporal precision of the approach in phantoms and *in vivo*.

Data acquired in stable phantoms showed high precision for the LED-based PAI system. COVs across both wavelengths studied were found to be less than 2% over 6 hours (one day) and less than 7% over 30 days, indicating high potential for longitudinal imaging studies using the technology. A similar level of precision has been found in laser-based PAI systems and compares well with other modalities for small animal imaging [28]. Reflecting on the phantom studies, across all parameters tested the factors that made the greatest impact on the signal repeatability were phantom positioning (based on replacement studies), placement of excitation LEDs and number of averages (based on SNR/SBR studies). Molecular imaging capabilities of LED-based PAI were then tested to perform biological validation under *in vivo* conditions. The results of our oxygen enhanced study clearly indicated the potential of the system to measure changes in blood oxygenation. The ability of the system to perform dynamic contrast enhanced studies of the kinetics of exogenously administered contrast agents was also assessed. The sensitivity for detection of ICG was lower than previously reported for laser-based systems, being 5 μM rather than 100 nM at 1 cm depth. Nonetheless, our findings indicate that the system is able to detect the dynamics of ICG *in vivo* and encouragingly the results closely match with a previous study conducted using laser-based PAI [35]. The implication of our findings is that LED-based PAI can

operate at high precision for real-time structural, functional and molecular imaging, which is important for biomedical applications in small animal models.

Several limitations exist in our study. Firstly, the LED-based PAI system under test is designed for handheld operation. To evaluate purely the system precision, we designed a custom gantry for application to phantoms and small animals, to minimize the influence of probe positioning and hence operator expertise. Future studies should compare these findings to data acquired under handheld conditions with different operators, to further assess the influence of these factors. Secondly, data acquired at 750 nm and 850 nm were used to evaluate the relative oxygenation of the hemoglobin, however, in the absence of fluence corrections, spectral coloring effects in tissue at depth were likely to have impacted the quantification of oxygenation, hence it being denoted in this study as a relative SO_2^{PAI} rather than absolute sO_2.

Conclusion

In summary, we performed technical and biological validation of a dual-wavelength LED-based PA / US imaging system. Our studies show that the dual-wavelength imaging capability of the system offers excellent precision in phantoms. The system is also capable of mapping changes in blood oxygenation levels and uptake of exogenous contrast agents. Thus, high power light emitting diodes (LEDs) can serve as fast, robust and cheap excitation sources for PAI *in vivo* based on both endogenous and exogenous molecular contrast, yielding a promising alternative to laser-based systems in biomedical applications.

Acknowledgements

This work was funded by PreXion Corporation through a grant to the University of Cambridge. Additional funding was provided through Cancer Research UK under grant numbers C14303/A17197, C9545/A29580, C47594/A16267, and C197/A16465 as well as the EPSRC (EP/R003599/1). We thank the workshop of the Department of Physics for their fabrication of the custom water baths and holders, as well as the Biological Resources Unit

of the CRUK Cambridge Institute for their assistance in performing animal studies. We also thank Dr Joanna Brunker and Marcel Gehrung for their inputs in data processing.

Competing interests

JJ and SEB received research funding from PreXion Corporation, which (Photoacoustic imaging division) was later acquired by CYBERDYNE INC. MKAS and NS are employees of CYBERDYNE INC. JJ and SEB have previously received research funding from iThera Medical GmbH.

Data statement

Associated data for this manuscript can be obtained by visiting: https://doi.org/10.17863/CAM.57999.

References

[1] D.A. Mankoff, A definition of molecular imaging, Journal of Nuclear Medicine 48(6) (2007) 18N-21N.

[2] L.V. Wang, J. Yao, A practical guide to photoacoustic tomography in the life sciences, Nature methods 13(8) (2016) 627.

[3] A. Taruttis, V. Ntziachristos, Advances in real-time multispectral optoacoustic imaging and its applications, Nature photonics 9(4) (2015) 219.

[4] S. Manohar, D. Razansky, Photoacoustics: a historical review, Advances in optics and photonics 8(4) (2016) 586-617.

[5] K.S. Valluru, K.E. Wilson, J.K. Willmann, Photoacoustic imaging in oncology: translational preclinical and early clinical experience, Radiology 280(2) (2016) 332-349.

[6] S. Manohar, M. Dantuma, Current and future trends in photoacoustic breast imaging, Photoacoustics 16 (2019).

[7] A. Oraevsky, B. Clingman, J. Zalev, A. Stavros, W. Yang, J.R. Parikh, Clinical optoacoustic imaging combined with ultrasound for coregistered functional and anatomical mapping of breast tumors, Photoacoustics 12 (2018) 30-45.

[8] I. Steinberg, D.M. Huland, O. Vermesh, H.E. Frostig, W.S. Tummers, S.S. Gambhir, Photoacoustic clinical imaging, Photoacoustics 14 (2019) 77-98.

[9] J. Weber, P.C. Beard, S.E. Bohndiek, Contrast agents for molecular photoacoustic imaging, Nature methods 13(8) (2016) 639-650.

[10] M.R. Tomaszewski, M. Gehrung, J. Joseph, I. Quiros-Gonzalez, J.A. Disselhorst, S.E. Bohndiek, Oxygen-Enhanced and Dynamic Contrast-Enhanced Optoacoustic Tomography Provide Surrogate Biomarkers of Tumor Vascular Function, Hypoxia, and Necrosis, Cancer research 78(20) (2018) 5980-5991.

[11] A. Shah, N. Bush, G. Box, S. Eccles, J. Bamber, Value of combining dynamic contrast enhanced ultrasound and optoacoustic tomography for hypoxia imaging, Photoacoustics 8 (2017) 15-27.

[12] A. Ron, X.L. Deán-Ben, S. Gottschalk, D. Razansky, Volumetric optoacoustic imaging unveils high-resolution patterns of acute and cyclic hypoxia in a murine model of breast cancer, Cancer research (2019) 3769.2018.

[13] Y. Wu, S. Huang, J. Wang, L. Sun, F. Zeng, S. Wu, Activatable probes for diagnosing and positioning liver injury and metastatic tumors by multispectral optoacoustic tomography, Nature communications 9(1) (2018) 3983.

[14] K. Pu, A.J. Shuhendler, J.V. Jokerst, J. Mei, S.S. Gambhir, Z. Bao, J. Rao, Semiconducting polymer nanoparticles as photoacoustic molecular imaging probes in living mice, Nature nanotechnology 9(3) (2014) 233.

[15] Y.-S. Chen, Y. Zhao, S.J. Yoon, S.S. Gambhir, S. Emelianov, Miniature gold nanorods for photoacoustic molecular imaging in the second near-infrared optical window, Nature nanotechnology 14(5) (2019) 465-472.

[16] Y.-S. Chen, W. Frey, S. Kim, K. Homan, P. Kruizinga, K. Sokolov, S. Emelianov, Enhanced thermal stability of silica-coated gold nanorods for photoacoustic imaging and image-guided therapy, Optics express 18(9) (2010) 8867-8878.

[17] Y.-S. Chen, W. Frey, S. Kim, P. Kruizinga, K. Homan, S. Emelianov, Silica-coated gold nanorods as photoacoustic signal nanoamplifiers, Nano letters 11(2) (2011) 348-354.

[18] M. Erfanzadeh, Q. Zhu, Photoacoustic imaging with low-cost sources; A review, Photoacoustics (2019) 1-11.

[19] A. Fatima, K. Kratkiewicz, R. Manwar, M. Zafar, R. Zhang, B. Huang, N. Dadashzadesh, J. Xia, M. Avanaki, Review of cost reduction methods in photoacoustic computed tomography, Photoacoustics (2019) 100137.
[20] S. Agrawal, C. Fadden, A. Dangi, X. Yang, H. Albahrani, N. Frings, S. Heidari Zadi, S.-R. Kothapalli, Light-Emitting-Diode-Based Multispectral Photoacoustic Computed Tomography System, Sensors 19(22) (2019) 4861.
[21] W. Xia, M. Kuniyil Ajith Singh, E. Maneas, N. Sato, Y. Shigeta, T. Agano, S. Ourselin, S. J West, A. E Desjardins, Handheld real-time LED-based photoacoustic and ultrasound imaging system for accurate visualization of clinical metal needles and superficial vasculature to guide minimally invasive procedures, Sensors 18(5) (2018) 1394.
[22] A. Hariri, J. Lemaster, J. Wang, A.S. Jeevarathinam, D.L. Chao, J.V. Jokerst, The characterization of an economic and portable LED-based photoacoustic imaging system to facilitate molecular imaging, Photoacoustics 9 (2018) 10-20.
[23] Y. Zhu, G. Xu, J. Yuan, J. Jo, G. Gandikota, H. Demirci, T. Agano, N. Sato, Y. Shigeta, X. Wang, Light emitting diodes based photoacoustic imaging and potential clinical applications, Scientific reports 8(1) (2018) 9885.
[24] T.J. Allen, P.C. Beard, High power visible light emitting diodes as pulsed excitation sources for biomedical photoacoustics, Biomedical optics express 7(4) (2016) 1260-1270.
[25] F.K. Joseph, M. Xavierselvan, M.K.A. Singh, S. Mallidi, C. Van Der Laken, F. Van De Loo, W. Steenbergen, LED-based photoacoustic imaging for early detection of joint inflammation in rodents: Towards achieving 3Rs in rheumatoid arthritis research, Photons Plus Ultrasound: Imaging and Sensing 2020, International Society for Optics and Photonics, 2020, p. 112400M.
[26] A. Hariri, K. Alipour, Y. Mantri, J.P. Schulze, J.V. Jokerst, Deep learning improves contrast in low-fluence photoacoustic imaging, Biomedical optics express 11(6) (2020) 3360-3373.
[27] S.R. Miri Rostami, M. Mozaffarzadeh, M. Ghaffari-Miab, A. Hariri, J. Jokerst, GPU-accelerated double-stage delay-multiply-and-sum algorithm for fast photoacoustic tomography using LED excitation and linear arrays, Ultrasonic imaging 41(5) (2019) 301-316.
[28] J. Joseph, M.R. Tomaszewski, I. Quiros-Gonzalez, J. Weber, J. Brunker, S.E. Bohndiek, Evaluation of precision in optoacoustic tomography for preclinical imaging in living subjects, Journal of Nuclear Medicine 58(5) (2017) 807-814.
[29] R. Bulsink, M. Kuniyil Ajith Singh, M. Xavierselvan, S. Mallidi, W. Steenbergen, K.J. Francis, Oxygen Saturation Imaging Using LED-Based Photoacoustic System, Sensors 21(1) (2021) 283.
[30] M. Jaeger, S. Schüpbach, A. Gertsch, M. Kitz, M. Frenz, Fourier reconstruction in optoacoustic imaging using truncated regularized inverse k-space interpolation, Inverse Problems 23(6) (2007) S51.
[31] S.E. Bohndiek, S. Bodapati, D. Van De Sompel, S.-R. Kothapalli, S.S. Gambhir, Development and application of stable phantoms for the evaluation of photoacoustic imaging instruments, PloS one 8(9) (2013).
[32] W.C. Vogt, C. Jia, K.A. Wear, B.S. Garra, T.J. Pfefer, Biologically relevant photoacoustic imaging phantoms with tunable optical and acoustic properties, Journal of biomedical optics 21(10) (2016) 101405.
[33] M. Fonseca, B. Zeqiri, P. Beard, B. Cox, Characterisation of a phantom for multiwavelength quantitative photoacoustic imaging, Physics in Medicine & Biology 61(13) (2016) 4950.

[34] T. Ishizawa, K. Masuda, Y. Urano, Y. Kawaguchi, S. Satou, J. Kaneko, K. Hasegawa, J. Shibahara, M. Fukayama, S. Tsuji, Mechanistic background and clinical applications of indocyanine green fluorescence imaging of hepatocellular carcinoma, Annals of surgical oncology 21(2) (2014) 440-448.
[35] A. Taruttis, S. Morscher, N.C. Burton, D. Razansky, V. Ntziachristos, Fast multispectral optoacoustic tomography (MSOT) for dynamic imaging of pharmacokinetics and biodistribution in multiple organs, PloS one 7(1) (2012) e30491.
[36] J. Laufer, C. Elwell, D. Delpy, P. Beard, In vitro measurements of absolute blood oxygen saturation using pulsed near-infrared photoacoustic spectroscopy: accuracy and resolution, Physics in Medicine & Biology 50(18) (2005) 4409.

Figures and Legends

Figure 1: Schematic of gantry and custom water baths for LED-based photoacoustic (PA) and ultrasound (US) imaging precision evaluation. (A) 3D gantry enables careful probe positioning with (x,y,z) control in a custom water bath. (B) For phantom imaging, a specific phantom holder was placed within the custom water bath from above. (C) For animal imaging, the custom water bath was placed above the animal, which was maintained on a heat pat underneath the holder and coupled with a polyethylene membrane (D).

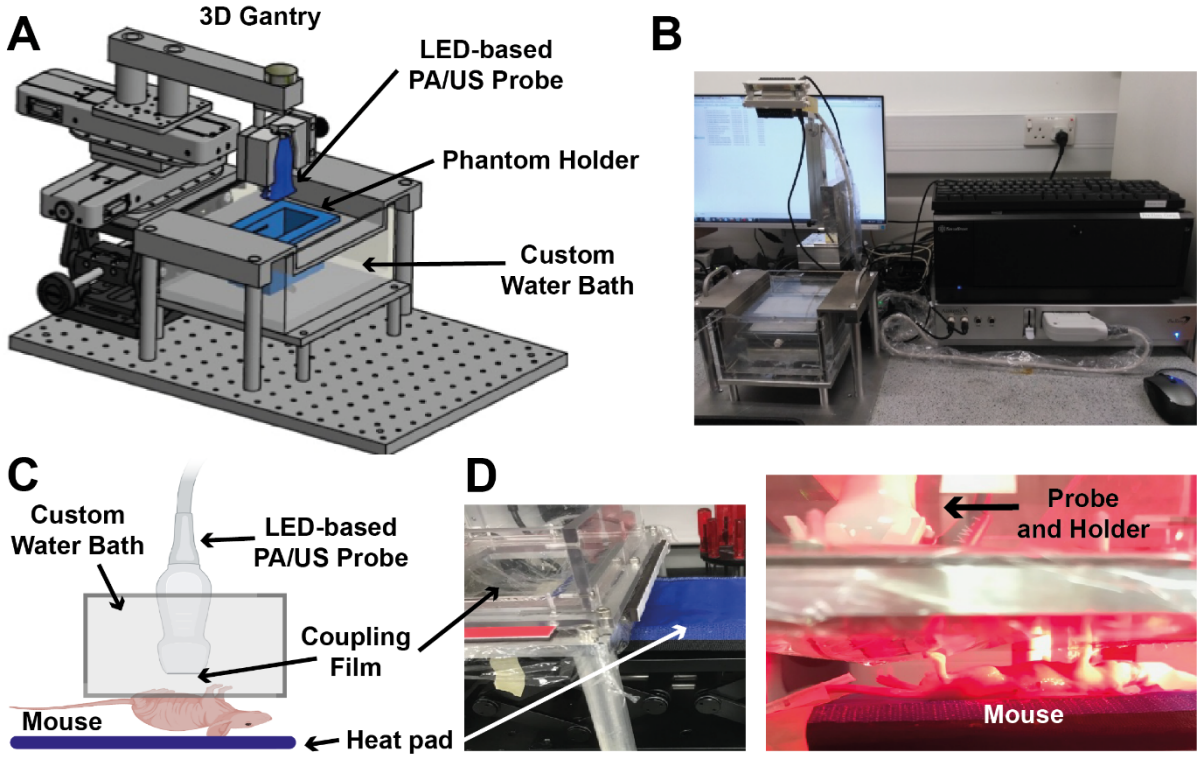

Figure 2: LED-based PAI exhibits high temporal precision in phantom imaging. (A) Photo (top) and PA image (bottom) of the PVCP phantom used for stability studies. Target inclusions are indicated with arrows. Mean pixel intensity values extracted from regions of interest (exemplars shown in dotted lines in A) were examined for continual acquisition over 180 minutes (B), repeated acquisitions over 30 days (C) and over 6 hours with (D) and without (E) replacement. Replacement indicates removal of the phantom from the imaging system in between measurements. Error bars are within the symbols. The gradient of the linear fits to the data for the 850 nm LED (black) and 750 nm LED (red) are given within each panel; none of the gradients are significantly non-zero.

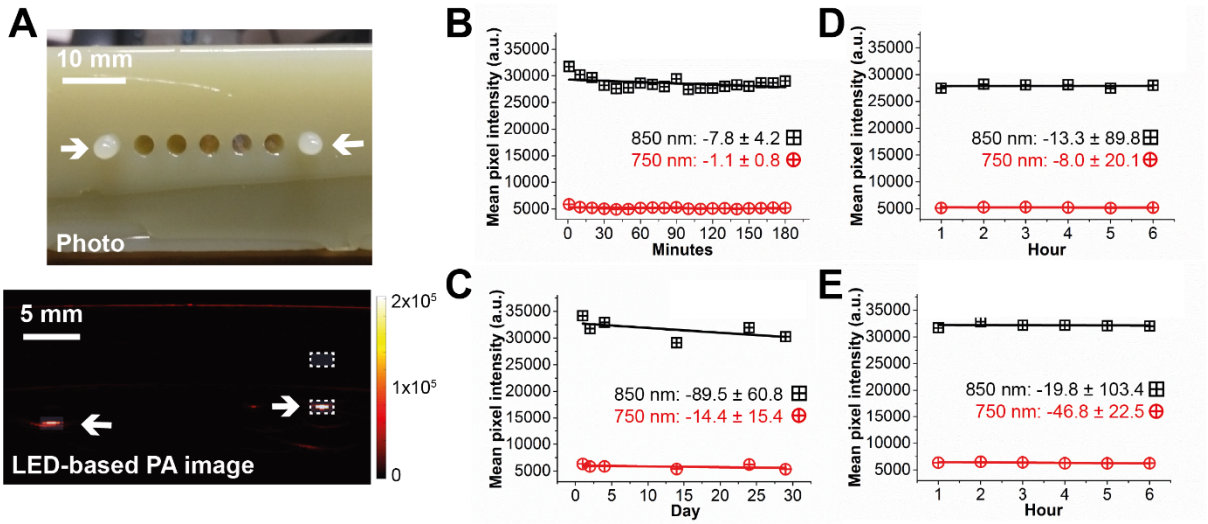

Figure 3: Impact of frame averaging on image quality in phantoms. Imaging signal-to-noise ratio (SNR) and signal to background ratio (SBR) increase as a function of the number of frame averages at 750 nm (A,B) and 850 nm (C,D). Error bars are within the symbols.

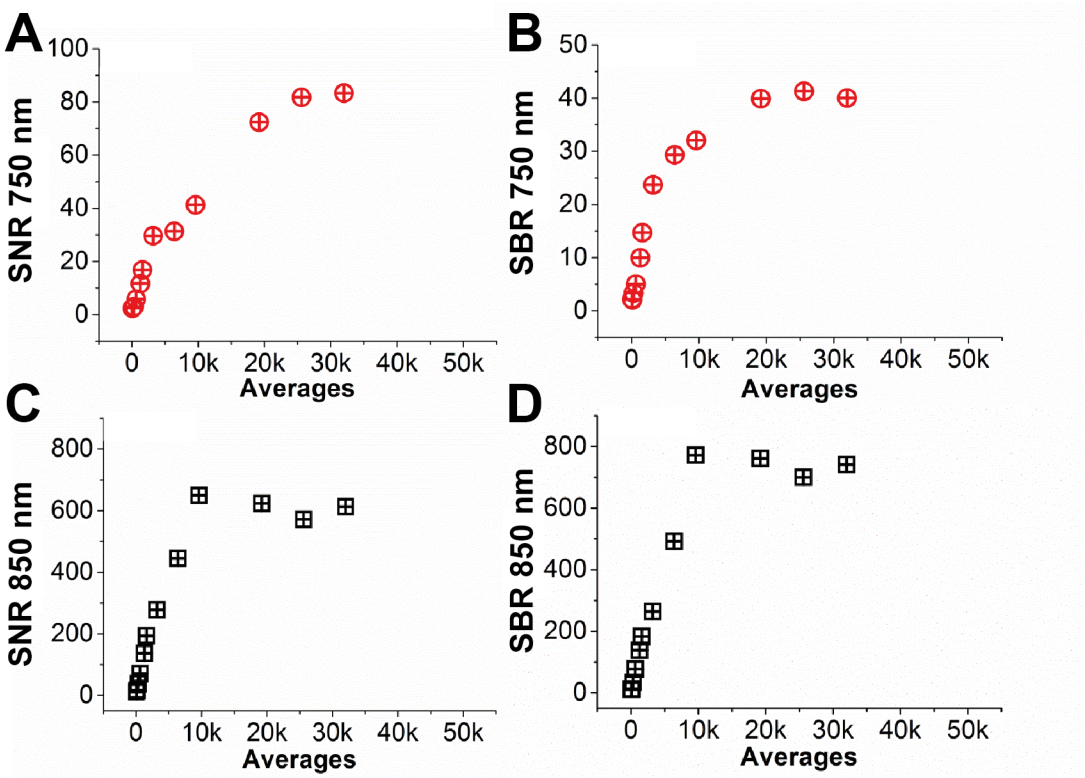

Figure 4: LED-based PAI is sensitive to an oxygen enhanced breathing gas challenge in the liver. (A) PA images obtained from the liver region with the mouse breathing either medical air (21% oxygen) or 100% oxygen gas. Region of interest for quantification shown as a dashed white ellipse. (B) Exemplar graph of the extracted SO_2^{PAI} over time in one mouse over 3 cycles of oxygen enhancement.

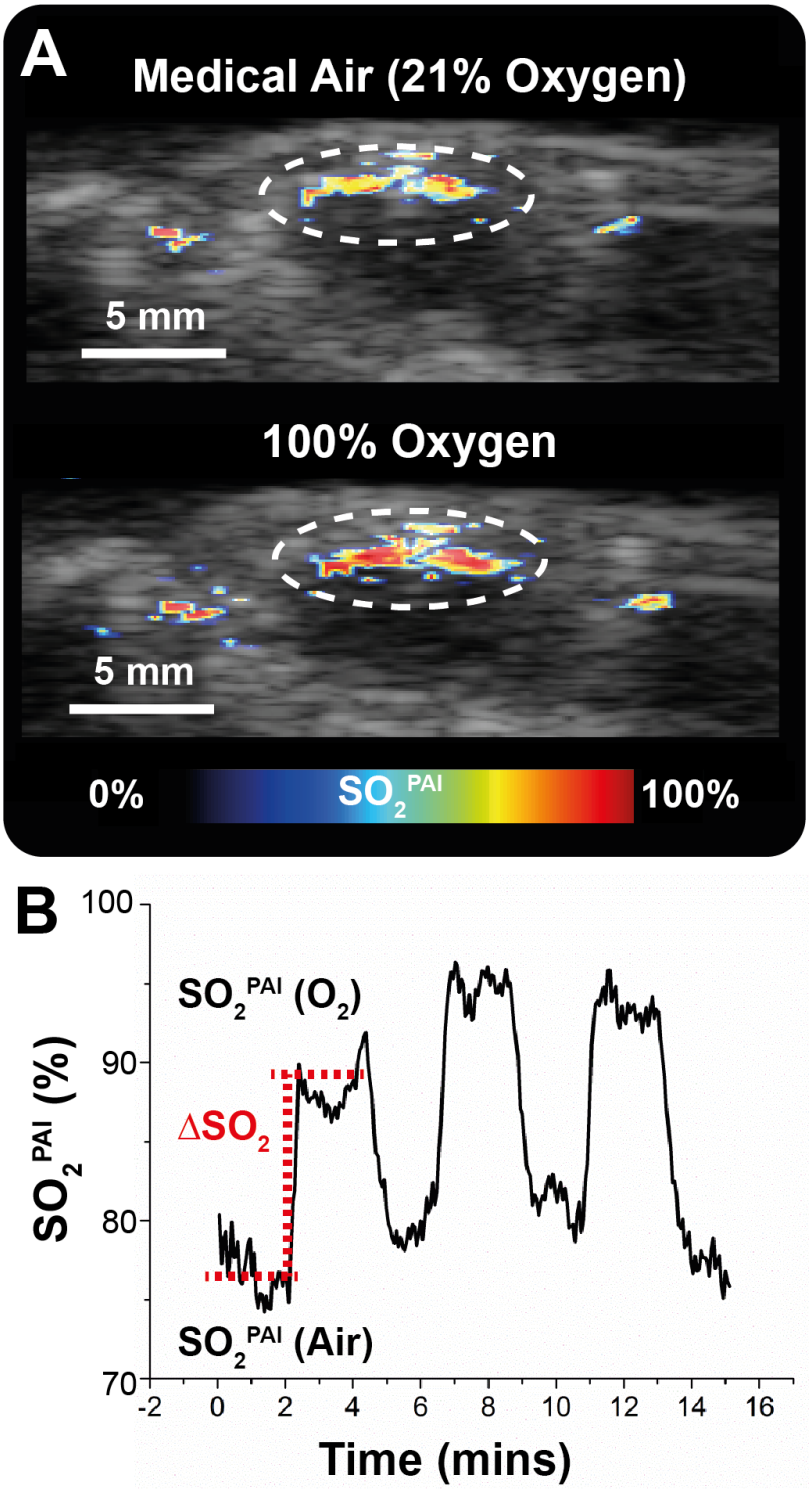

Figure 5: LED-based PAI shows accumulation of indocyanine green over time. (A) PA images obtained from the liver region before (pre-injection) and 9 mins after (post injection) intravenous administration of indocyanine green. Region of interest for quantification shown as a dashed white ellipse. (B) Exemplar graph of the normalized mean pixel intensity (MPI) showing the dynamic contrast enhancement over time.

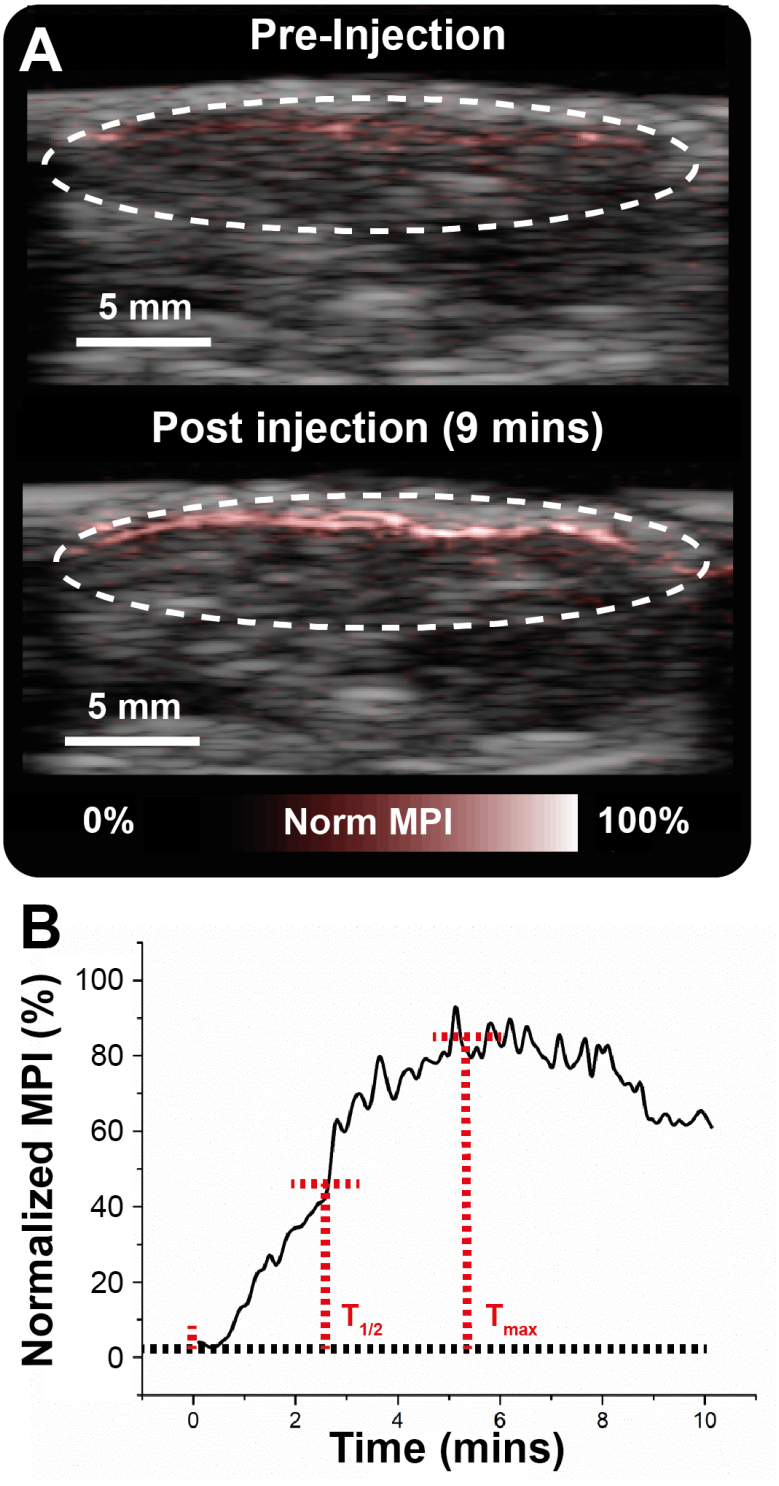

Table 1 Summary of the dynamics of SO_2^{PAI} over time under multiple breathing cycles measured from the oxygen challenge studies.

OE Direction	Single Mouse			Both Mice		
	ΔSO_2	% COV SO_2 (Air)	% COV SO_2 (O_2)	ΔSO_2	% COV SO_2 (Air)	% COV SO_2 (O_2)
Air to O_2	0.16 ± 0.01	2.9	3.5	0.18 ± 0.02	7.6	10
O_2 to Air	0.14 ± 0.02			0.23 ± 0.05		

Movie 1 Photoacoustic and ultrasound data during the air breathing phase of the oxygen challenge.

Movie 2 Photoacoustic and ultrasound data during the oxygen breathing phase of the oxygen challenge.